JACS
JOURNAL OF THE AMERICAN CHEMICAL SOCIETY
Article
pubs.acs.org/JACS

Raising the Thermoelectric Performance of p-Type PbS with Endotaxial Nanostructuring and Valence-Band Offset Engineering Using CdS and ZnS

Li-Dong Zhao,[†] Jiaqing He,[†,‡] Shiqiang Hao,[‡] Chun-I Wu,[§] Timothy P. Hogan,[§] C. Wolverton,[‡] Vinayak P. Dravid,[‡] and Mercouri G. Kanatzidis*[,†]

[†]Department of Chemistry and [‡]Department of Materials Science and Engineering, Northwestern University, Evanston, Illinois 60208, United States

[§]Department of Electrical and Computer Engineering, Michigan State University, East Lansing, Michigan 48824, United States

Supporting Information

ABSTRACT: We have investigated in detail the effect of CdS and ZnS as second phases on the thermoelectric properties of p-type PbS. We report a ZT of ∼1.3 at 923 K for 2.5 at.% Na-doped p-type PbS with endotaxially nanostructured 3.0 at.% CdS. We attribute the high ZT to the combination of broad-based phonon scattering on multiple length scales to reduce (lattice) thermal conductivity and favorable charge transport through coherent interfaces between the PbS matrix and metal sulfide nanophase precipitates, which maintains the requisite high carrier conductivity and the associated power factor. Similar to large ionically bonded metal sulfides (ZnS, CaS, and SrS), the covalently bonded CdS can also effectively reduce the lattice thermal conductivity in p-type PbS. The presence of ubiquitous nanostructuring was confirmed by transmission electron microscopy. Valence and conduction band energy levels of the NaCl-type metal sulfides, MS (M = Pb, Cd, Zn, Ca, and Sr) were calculated from density functional theory to gain insight into the band alignment between PbS and the second phases in these materials. The hole transport is controlled by band offset minimization through the alignment of valence bands between the host PbS and the embedded second phases, MS (M = Cd, Zn, Ca, and Sr). The smallest valence band offset of about 0.13 eV at 0 K was found between PbS and CdS which is diminished further by thermal band broadening at elevated temperature. This allows carrier transport between the endotaxially aligned components (i.e., matrix and nanostructure), thus minimizing significant deterioration of the hole mobility and power factor. We conclude the thermoelectric performance of the PbS system and, by extension, other systems can be enhanced by means of a closely coupled phonon-blocking/electron-transmitting approach through embedding endotaxially nanostructured second phases.

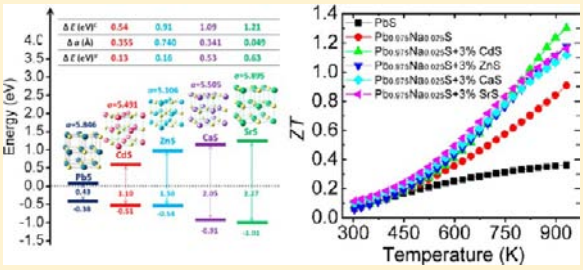

INTRODUCTION

Solid-state thermoelectric generation technology, capable of creating electricity from waste heat sources, is expected to play a role in energy efficiency and augment conventional and alternative energy sources by harvesting waste heat and converting it into electricity. The efficiency of thermoelectric materials and devices is quantified by the dimensionless figure of merit (ZT), defined as $ZT = (S^2\sigma/\kappa)T$, where S, σ, κ, and T are the Seebeck coefficient, electrical conductivity, thermal conductivity, and absolute temperature, respectively.[1,2] The interdependence of S, σ, and κ complicates efforts in developing strategies for improving a material's average ZT above 3, a feat that could revolutionize the field of energy conversion. Generally, the most successful route to enhance ZT is reducing the thermal conductivity particularly through nanostructuring.[1,2] Typical examples are embedding nanoscale precipitates in bulk materials that scatter heat-carrying phonons, e.g., $AgPb_mSbTe_{m+2}$,[3−5] $AgPb_mSn_nSbTe_{2+m+n}$,[6] $NaPb_mSbTe_{2+m}$,[7] PbTe−PbS,[8] PbTe−CdTe,[9] PbSe−PbS,[10] PbS−PbTe,[11] PbS−Bi_2S_3/Sb_2S_3,[12] PbS−SrS/CaS,[13] nano-SiC in Bi_2Te_3,[14] Yb_2O_3 in $CoSb_3$,[15] Pb/Sb in PbTe,[16] Sb in $YbCoSb_{12}$,[17] and ErAs in $In_{0.53}Ga_{0.47}As$.[18] In all these cases, however, the power factor is also reduced relative to the single-phase parent material because the nanoinclusions increase carrier scattering. Therefore, the challenge to develop materials with superior performance is to tailor the interconnected thermoelectric physical parameters for a crystalline system.

Epitaxial superlattice thin films of Bi_2Te_3/Sb_2Te_3 were reported to be capable of allowing carriers to transmit via small band offsets while reducing thermal conductivity by acoustic mismatch between the superlattice components.[19] This phonon-blocking/electron-transmitting approach also has been realized in bulk systems. It has been observed that the heat flow can be greatly inhibited without affecting the carrier mobility by embedding endotaxial SrTe nanocrystals in p-type PbTe.[20] The insensitivity of carrier scattering was attributed to valence band alignment of SrTe and PbTe, allowing facile hole transport. The

Received: July 4, 2012
Published: September 19, 2012

   dx.doi.org/10.1021/ja306527n | J. Am. Chem. Soc. 2012, 134, 16327−16336

lattice mismatch of SrTe and PbTe and associated strain at interfaces decouples phonon and hole transport leading to a ZT of 1.7 at ∼800 K.[20]

Recently, we proposed that PbS is an ideal candidate for widespread application of environmentally stable and affordable thermoelectric material system because high performance in both n-type (ZT ∼ 1.1 at 923 K)[12] and p-type (ZT ∼ 1.1 at 923 K)[13] can be achieved. Sulfur is very earth-abundant compared to Te and Se, and the Pb is extremely strongly bound, making it environmentally safe.[11−13] In our previous studies we showed that the lattice thermal conductivity can be reduced to very low levels through nanostructuring with metal sulfides (Bi_2S_3 and Sb_2S_3 in n-type,[12] SrS and CaS in p-type[13]). However, the carrier mobility is somewhat deteriorated by these nanoprecipitates compared to the pure PbS matrix. The above-mentioned approach associated with endotaxial SrTe nanostructures in PbTe[20] prompted us to investigate the thermoelectric properties of PbS embedded with nanocrystals of other metal sulfides, especially those with more narrow band gaps than CaS and SrS. In the present paper we hypothesized that valence band alignment achieved with suitable metal sulfides and PbS could suppress hole scattering in p-type PbS by reducing hole transport barriers at the matrix/nanostructure interface. We demonstrate here that this indeed can be achieved and the ZT can be further increased to ∼1.3 at 923 K in p-type PbS with CdS nanostructures. Although the same strong reduction of the lattice thermal conductivity is achieved with SrS and CaS,[13] the enhanced ZT of the CdS system derives from better hole mobility because of the smaller band offsets between the valence bands in the two component materials. This explanation is supported by first-principles density functional theory calculations of the relative band energy levels for these metal sulfides, MS (M = Pb, Cd, Zn, Ca, and Sr). The present results confirm that higher thermoelectric performance can be realized in bulk p-type PbS with endotaxial placement of second phases coupled with electronic valence band alignment.

EXPERIMENTAL SECTION

Reagents. Pb wire (99.99%, American Elements, US), S shot or chunk (99.999%, 5 N Plus, Canada), Zn powder (99.99%, Baker, US), Cd powder (99.99%, Alfa, US), and Na chunk (99.999%, Aldrich, Milwaukee, WI).

Synthesis. Ingots (∼20 g) with nominal compositions of PbS with x% ZnS/CdS (mole fraction in the text, x = 0, 1, 2, 3, and 4) and with 2.5% Na dopant were synthesized by mixing appreciated ratios of high purity starting materials of Pb, S, Zn/Cd, and Na in carbon-coated quartz tubes under an N_2-filled glovebox. The tubes were then evacuated to a pressure of ∼10^{-4} Torr, flame-sealed, slowly heated to 723 K in 12 h and then to 1423 K in 7 h, soaked at this temperature for 6 h, and subsequently water-quenched to room temperature. The obtained ingots were crushed into powders and then densified by spark plasma sintering (SPS) (SPS-10-4, Thermal Technology). Highly dense samples can achieve ∼93% of theoretical density. To prepare for SPS processing, the melt-grown ingots were ground to powder using a mortar and pestle to reduce the grain size to smaller than 5 mm^3 and then further ground by a mechanical mortar and pestle to reduce the grains to less than 53 μm^3. These powders were then densified at 723 K for 10 min in a 20 mm diameter graphite die under an axial compressive stress of 60 MPa in an argon atmosphere. Highly dense disk-shaped pellets with dimensions of ⌀ 20 mm × 9 mm were obtained. The manipulations and preparative steps for grinding powders for SPS were carried out in a purified Ar-atmosphere glovebox.

Energy Band Gaps. Room temperature optical diffuse reflectance measurements were performed on finely ground powders to probe optical energy gap of the series. The spectra were collected in the mid-IR range (6000−400 cm^{-1}) using a Nicolet 6700 FT-IR spectrometer.[11,20] The reflectance versus wavelength data generated were used to estimate the band gap by converting reflectance to absorption data according to Kubelka−Munk equations: $\alpha/S = (1 - R)^2/2R$, where R is the reflectance and α and S are the absorption and scattering coefficients, respectively.

Electrical Properties. The obtained SPS processed pellets were cut into bars with dimensions 18 mm × 3 mm × 3 mm that were used for simultaneous measurement of the Seebeck coefficient and the electrical conductivity using an Ulvac Riko ZEM-3 instrument under a helium atmosphere from room temperature to 923 K. The samples were coated with a thin layer (0.1−0.2 mm) of boron nitride (BN) to protect the instruments.[12,13] Heating and cooling cycles gave repeatable electrical properties to verify the thermal stability. Electrical properties obtained from different slices cut from the same pellets were similar, attesting to the homogeneity of the samples. The uncertainty of the Seebeck coefficient and electrical conductivity measurements is 5%.

Hall Measurements. Hall coefficients were measured on a home-built system in magnetic fields ranging from 0 to 1.25 T, utilizing simple four-contact Hall-bar geometry, in both negative and positive polarity to eliminate Joule resistive errors.[10−13]

Thermal Conductivity. High density SPS processed pellets were cut and polished into coins of ⌀ ∼8 mm and 1−2 mm thickness for thermal diffusivity measurements. The samples were coated with a thin layer of graphite to minimize errors from the emissivity of the material. The thermal conductivity was calculated from $\kappa = DC_p\rho$, where the thermal diffusivity coefficient (D) was measured using the laser flash diffusivity method in a Netzsch LFA457, the specific heat capacity (C_p) was indirectly derived using a representative sample (Pyroceram 9606) in the range 300−923 K, and the density (ρ) was determined using the dimensions and mass of the sample, which was then reconfirmed using a gas pycnometer (Micromeritics AccuPyc1340) measurements. The thermal diffusivity data were analyzed using a Cowan model with pulse correction,[11−13] and heating and cooling cycles give reproducible values for each sample. The C_p results show good agreement with the reported values.[21] Thermal diffusivities obtained for different slices from the same pellet are also similar. The uncertainty of the thermal conductivity is estimated to be within 8%, considering the uncertainties for D, C_p, and ρ. The combined uncertainty for all measurements involved in the calculation of ZT is less than 15%. No directional anisotropy effects were observed in the charge transport properties through measurements in transverse and longitudinal directions. The thermal diffusivity, density, and the heat capacity data for all samples can be found in the Figure S3, Table S1, and Figure S6 (Supporting Information).

Electron Microscopy and X-ray Diffraction. Transmission electron microscopy (TEM) investigations were carried out in a JEOL 2100F microscope operated at 200 kV. The thin TEM specimens were prepared by conventional methods and include cutting, grinding, dimpling, polishing, and Ar-ion milling on a liquid N_2 cooling stage. Samples pulverized with an agate mortar were used for powder X-ray diffraction (XRD). The powder diffraction patterns were obtained with Cu K_α (λ = 1.5418 Å) radiation in a reflection geometry on an Inel diffractometer operating at 40 kV and 20 mA and equipped with a position-sensitive detector.

Band Gap Calculations. Density functional theory (DFT) electronic structure calculations of the NaCl-type metal sulfides, PbS, CdS, ZnS, CaS, and SrS, were performed to gain insights into the various band alignments in these materials. Here, it is worth noting that the rock salt structure of the PbS matrix could impose the NaCl structure on the small CdS and ZnS precipitates, an effect that is well-known in metallurgy. The calculations were performed using the generalized gradient approximation with the PBE[22] functional for the exchange correlation functional and projector-augmented wave potentials as implemented in VASP (Vienna Ab-initio Simulation Package).[23] All structures are fully relaxed with respect to cell vectors and cell-internal positions. The electronic DOS (density of states) is calculated from the relaxed structures using the tetrahedron method

with Blöchl corrections. For the Pb, Ca, and Sr species, the 5d, 3p, and 4s electrons are treated as valence states, respectively. The zone samplings are performed using a 16 × 16 × 16 *k*-point mesh for PbS, SrS, CaS, ZnS, and CdS, respectively. To assess the relative band alignments of the various second-phase materials with those of PbS, we utilize the findings of Van de Walle and Neugebauer, who demonstrated a universal alignment of the electronic transition level of hydrogen in a wide range of materials including semiconductors, insulators, and even aqueous solutions[24] (details are given in Supporting Information). Hence, to infer the band alignment, we compute the energies of H defects in the rock salt compounds of interest, assume alignment between these H energies, and then extract the band alignment of the compounds. To align the valence band maximum position of each system, we consider the defect formation energies of various charge states of interstitial H^q ($q = -1, 0, 1$) by placing H in the host material with a 128 atom supercell, calculating the total energy of this structure, and subtracting the energy of the corresponding pure host material, hydrogen chemical potential, and electron chemical potential:[24]

$$\Delta E^f(H^q) = E_{tot}(H^q) - E_{tot}(\text{bulk}) - 0.5E_{tot}(H_2) + q(E_V + \Delta E + E_F)$$

where E_V and E_F are valence band maximum and Fermi level (relative to the VBM). To select the most favorable interstitial H binding sites in host materials, multiple binding configurations are calculated. The electrostatic potential correction term ΔE is calculated by inspecting the potential in the supercell far from the impurity and aligning it with the electrostatic potential in bulk.[25] The calculation details can be found in Figures S8 and Figure S9, Supporting Information.

RESULTS AND DISCUSSION

ZnS and CdS were chosen for investigation as a follow up to our recent study on the CaS and SrS systems.[13] ZnS and CdS present several substantial chemical and physical differences from the alkaline earth sulfides. Key differences include the following: (a) the M−S bonding is much more covalent in ZnS and CdS than in CaS and SrS; (b) the energy band gaps are much narrower in ZnS and CdS; (c) the energies of the conduction and valence band levels are different, thereby presenting opportunities for band alignment engineering in connection with those of PbS. These parameters are critical to the thermoelectric properties of the nanostructured materials, and studying them could allow us to delineate their roles in the charge and thermal transport in the matrix of PbS.

Powder XRD patterns of the PbS samples containing ZnS show a single phase that can be indexed to the NaCl structure type up to 4.0% ZnS, Figure S1 in Supporting Information. No ZnS or other phases were observed within the detection limits of the measurements; the inset lattice parameters experience negligible changes with the added ZnS fractions. With an increase in the ZnS concentration the electronic absorption spectra of the PbS samples, without any Na doping, show only a small shift of the absorption edge toward higher energy (Figure S2, Supporting Information). The band gaps derived from the plots show a slight increase from ∼0.43 eV to ∼0.44 eV in going from 1.0% to 4.0% ZnS in PbS, inset in Figure S2. Generally, if ZnS was forming a solid solution with PbS, one would expect a Vegard's law type behavior, showing a systematic increase in the band gap with the amount of ZnS, inset in Figure S2. Such a small increase in the band gap with the addition of a wide band gap metal sulfide such as ZnS in a narrow band gap PbS (∼0.43 eV) suggests that the majority of ZnS is excluded from the PbS matrix rather than forming a conventional solid solution.

Figure 1 shows the thermoelectric properties as a function of temperature for $Pb_{0.975}Na_{0.025}S$-*x*% ZnS. The electrical conductivities decrease with increasing temperature, as expected, and are lower for increasing amounts of ZnS over the entire temperature range. Specifically, the room temperature electrical conductivity significantly decreases from ∼1421Scm^{-1} for $Pb_{0.975}Na_{0.025}S$ to ∼489 Scm^{-1} for the sample with 4.0% ZnS. As shown in Figure 1b, the Seebeck coefficients are negative for pure "undoped" PbS and become positive with Na doping and acquire hole-dominated transport. The Seebeck coefficient at room temperature for pure PbS is ∼ −240 μV K^{-1}, and becomes positive e.g. ∼ +64 μV K^{-1} for the sample with 2.5% Na doping. With varying ZnS fraction, the Seebeck coefficients show negligible change, suggesting the carrier concentration, which is controlled by the Na concentration, is similar for all samples. Therefore, the rising fraction of ZnS as a second phase significantly diminishes the hole mobility as seen by the trend in the measured Hall mobility values listed in Table 1 and the room temperature electrical conductivity. The power factor of pure PbS shows a maximum value of ∼6.0 μW cm^{-1} K^{-2} around room temperature falling to ∼2.8 μW cm^{-1} K^{-2} at 923 K, Figure 1c. The maximum of the power factor shifts to higher temperature by the 2.5% Na doping and reaches the highest value of ∼10.4 μW cm^{-1} K^{-2} at 923 K. Compared to the "control" sample $Pb_{0.975}Na_{0.025}S$, the ZnS-containing samples show a decreasing trend for power factors at 923 K with rising ZnS fractions, ranging from ∼9.3 μW cm^{-1} K^{-2} to ∼10.2 μW cm^{-1} K^{-2}.

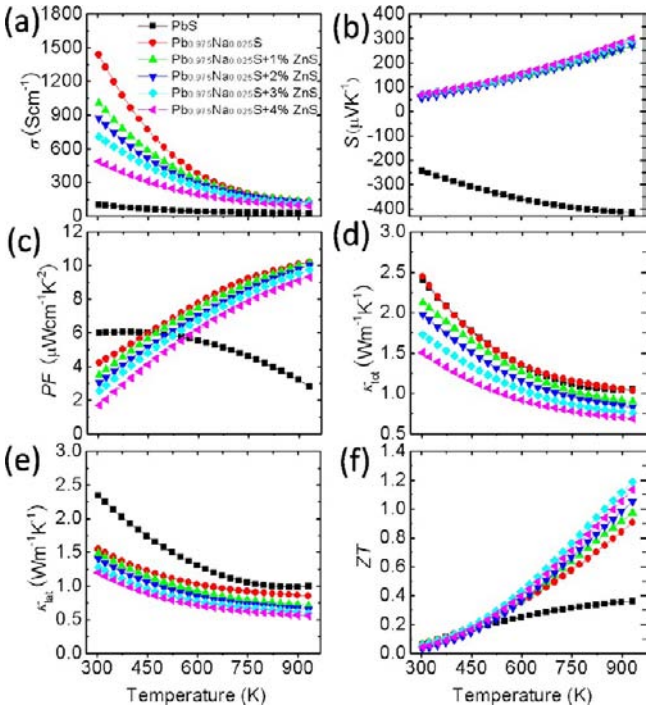

Figure 1. Thermoelectric properties as a function of temperature for $Pb_{0.975}Na_{0.025}S$ with *x*% ZnS: (a) Electrical conductivity. (b) Seebeck coefficient. (c) Power factor. (d) Total thermal conductivity. (e) Lattice thermal conductivity. (f) Figure of merit, *ZT*; the combined uncertainty for all measurements involved in the calculation of *ZT* is less than 15%.

The total thermal conductivity (κ_{tot}) shows a significant decrease with increasing ZnS, Figure 1d. κ_{tot} is the sum of the electronic (κ_{ele}) and lattice thermal conductivity (κ_{lat}). κ_{ele} is

dx.doi.org/10.1021/ja306527n | J. Am. Chem. Soc. 2012, 134, 16327−16336

Table 1. Transport Properties of p-Type PbS Polycrystallines[a]

samples	n_H (10^{19}cm^{-3})	r_H	μ_H (cm^{2}V^{-1}s^{-1})	S (μVK^{-1})	σ (Scm^{-1})	$m^*(m_o)$	κ_L (RT) (W m^{-1} K^{-1})	κ_L (923K) (W m^{-1} K^{-1})	ZT_{max} (923K)
PbS	0.40	1.16	277	−240	102	0.38	2.34	0.98	0.4
$Pb_{0.975}Na_{0.025}S$	4.78	1.04	186	65	1421	0.42	1.54	0.85	0.9
$Pb_{0.975}Na_{0.025}S$ + 1.0% ZnS	4.71	1.04	134	68	1007	0.44	1.48	0.71	1.0
$Pb_{0.975}Na_{0.025}S$ + 2.0%ZnS	4.81	1.03	114	55	874	0.40	1.40	0.66	1.1
$Pb_{0.975}Na_{0.025}S$ + 3.0% ZnS	4.78	1.05	93	70	708	0.46	1.28	0.60	1.2
$Pb_{0.975}Na_{0.025}S$ + 4.0% ZnS	4.79	1.05	64	70	489	0.46	1.20	0.56	1.1
$Pb_{0.975}Na_{0.025}S$ + 1.0% CdS	4.77	1.03	184	52	1407	0.36	1.50	0.74	1.1
$Pb_{0.975}Na_{0.025}S$ + 2.0% CdS	4.72	1.03	147	58	1107	0.38	1.49	0.69	1.2
$Pb_{0.975}Na_{0.025}S$ + 3.0% CdS	4.75	1.03	130	51	987	0.34	1.34	0.62	1.3
$Pb_{0.975}Na_{0.025}S$ + 4.0% CdS	4.72	1.04	113	62	854	0.40	1.22	0.58	1.2

[a] n_H, carrier concentration; r_H, Hall factor; μ_H, carrier mobility; S, Seebeck coefficient; σ, electrical conductivity; $m^*(m_o)$, the effective mass; κ_L, lattice thermal conductivity; ZT, the dimensionless figure of merit.

proportional to the electrical conductivity (σ) through the Wiedemann–Franz relation, $\kappa_{ele} = L\sigma T$, where L is the Lorenz number extracted as described previously by fitting of the respective Seebeck values (estimated from the reduced chemical potential) assuming a single band model and acoustic phonon scattering as the main carrier scattering mechanism ($r = -1/2$);[26] the calculation can be performed as explained in detail previously.[10−13] The heat capacity, thermal diffusivity, Lorenz number, and electronic thermal conductivity for $Pb_{0.975}Na_{0.025}S$-x%ZnS are shown in Figure S3. The total thermal conductivity shows a significant decrease with increasing ZnS, and this falling trend is also observed in the lattice thermal conductivity, Figure 1e, indicating that the dispersed ZnS phase is highly effective in scattering acoustic phonons. At room temperature, the lattice thermal conductivity decreases from ∼2.34 W m^{-1} K^{-1} for pure PbS to ∼1.48 W m^{-1} K^{-1} for the $Pb_{0.975}Na_{0.025}S$-1.0% ZnS, and to ∼1.2 W m^{-1} K^{-1} as the ZnS content is increased to 4.0%. Correspondingly, the lattice thermal conductivity at 923 K decreases to ∼0.71 W m^{-1} K^{-1} and ∼0.56 W m^{-1} K^{-1} for the 1.0% and 4.0% ZnS samples, respectively. As shown in Figure 1f, the ZT values for the ZnS-containing samples continue to rise up to 923 K. The maximum ZT value of ∼1.2 at 923 K is observed for the $Pb_{0.975}Na_{0.025}S$-3.0% ZnS sample; this value matches that of the $Pb_{0.975}Na_{0.025}S$-3.0% SrS.[13]

CdS has a narrower band gap and a larger lattice constant than that of ZnS, and therefore the addition of CdS into the PbS matrix is expected to present differences in the thermal and charge transport behavior arising from the different alignment of the valence band maxima for PbS/ZnS vs PbS/CdS. The PXRD patterns of $Pb_{0.975}Na_{0.025}S$-x% CdS show a single phase that can be indexed to the NaCl structure type regardless of CdS concentration (up to 4.0%), as shown in Figure S4, and the inset lattice parameters experience negligible changes with the added CdS fractions. As in the case of ZnS above, a small increase in the band gap with increasing CdS from 1.0% to 4.0% suggests that the majority of CdS is excluded from the PbS matrix instead of forming a conventional solid solution, Figure S5 in Supporting Information. Figure 2 shows that the electrical and thermal transport behavior for the $Pb_{0.975}Na_{0.025}S$-x% CdS sample are very similar to those of ZnS. The heat

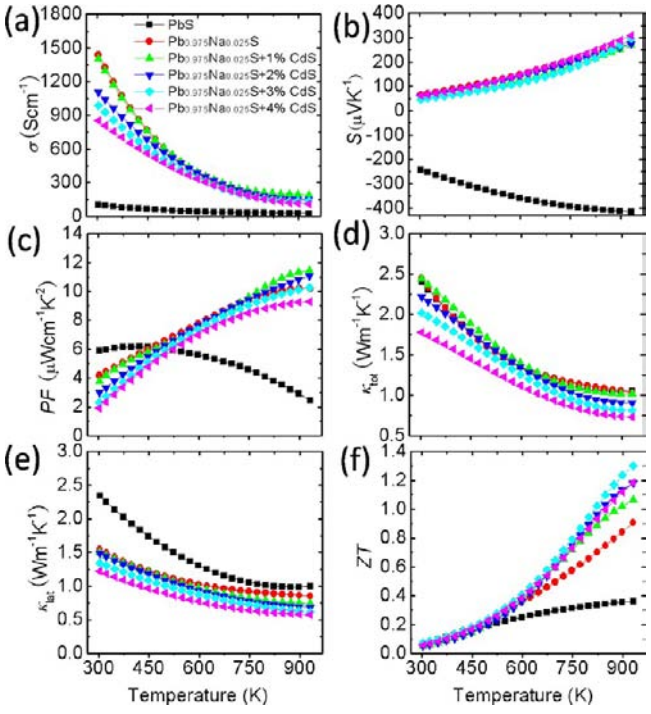

Figure 2. Thermoelectric properties as a function of temperature for $Pb_{0.975}Na_{0.025}S$ with x% CdS: (a) Electrical conductivity. (b) Seebeck coefficient. (c) Power factor. (d) Total thermal conductivity. (e) Lattice thermal conductivity. (f) Figure of merit, ZT; the combined uncertainty for all measurements involved in the calculation of ZT is less than 15%.

capacity, thermal diffusivity, Lorenz number, and electronic thermal conductivity for these samples can be found in Figure S6. The $Pb_{0.975}Na_{0.025}S$-3.0% CdS sample reaches a maximum ZT value of ∼1.3 at 923 K (Figure 2f), which is higher than that of the $Pb_{0.975}Na_{0.025}S$-3.0% ZnS sample. The improvement of ZT in the $Pb_{0.975}Na_{0.025}S$-x% CdS samples over those with ZnS, CaS,[13] and SrS[13] arises from the higher power factor, Figure 2d. These power factors are as high as those of $Pb_{0.975}Na_{0.025}S$ without second phases in the entire temperature range. The

dx.doi.org/10.1021/ja306527n | J. Am. Chem. Soc. 2012, 134, 16327−16336

power factors decrease from ~11.4 μW cm^{-1} K^{-2} to ~9.3 μW cm^{-1}K^{-2}, as the CdS rises from 1.0% to 4.0%, Figure 2c.

The well-established Pisarenko relation between the Seebeck coefficient and carrier concentration (assuming a parabolic band and an acoustic phonon scattering mechanism)[11−13] gives a good description of the experimental data, Figure 3. It is

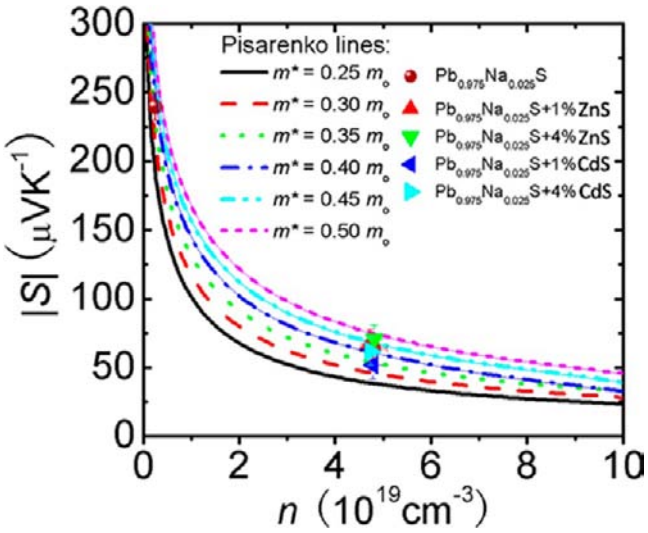

Figure 3. Pisarenko plots at 300 K. Seebeck coefficients as a function of carrier concentration. The lines correspond to the theoretically expected curves for the pristine PbS with $m^* \sim xm_o$ (x = 0.25, 0.30, 0.35, 0.40, 0.45, and 0.50). The excellent agreement suggests that Na doping levels and second phases (ZnS/CdS) have no marked effects in perturbing the electronic density of states of PbS.

noteworthy that the Seebeck coefficients for the $Pb_{0.975}Na_{0.025}S$ sample, as well as samples containing 1.0% and 4.0% ZnS/CdS, agree with that of pure PbS within the studied carrier concentration ranges. This agreement suggests that no particular enhancements of the Seebeck coefficient by resonant-state scattering or other mechanisms are operating after introducing these nanostructuring second phases. Therefore, the enhanced power factor for the CdS-containing samples compared to the ZnS-, CaS-, and SrS-containing samples arises from the higher electrical conductivity. Because the carrier concentration is similar in all these samples and controlled by fixing the Na doping, the reason for the higher electrical conductivity and thus in the enhancement of ZT is attributed to the carrier mobility, a conclusion that is well supported by the data listed in Table 1. In the next section, we will discuss how the hole carrier mobility is affected by the valence band alignment in the host PbS matrix and guest-embedded CdS nanophases.

To further illustrate the effects of metal sulfide nanophases on the thermoelectric properties of PbS, we make a comparison of the thermoelectric properties in the p-type PbS system with all relevant metal sulfides studied thus far, e.g., CdS, ZnS, CaS, and SrS. Figure 4 shows the thermoelectric properties as a function of temperature for $Pb_{0.975}Na_{0.025}S$ with 3.0% metal sulfides (CdS, ZnS, CaS, and SrS) because 3.0% is the optimized fraction for all systems resulting in the best thermoelectric performance in p-type PbS with Na doping.[13] It is readily seen from Figure 4a that the electrical conductivity for the CdS-containing sample outperforms all others over the entire measurement temperature range. Also it can clearly be seen from the enlarged plot of electrical conductivity in the

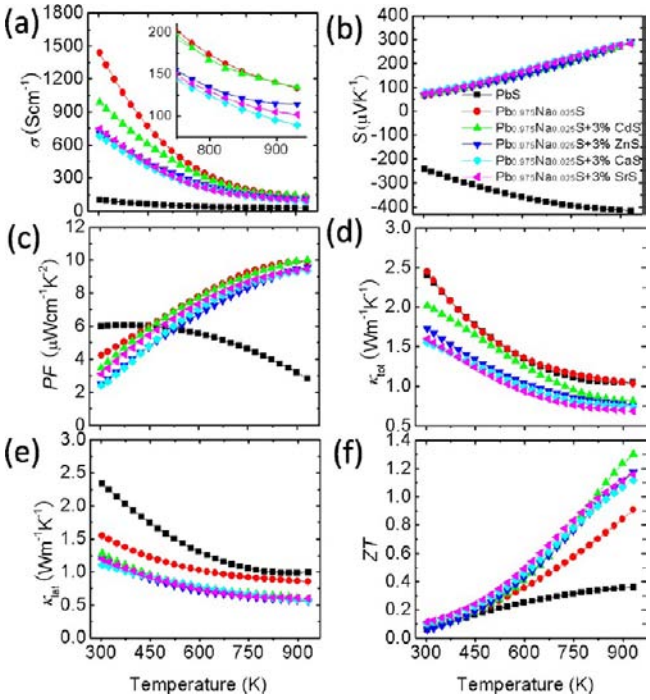

Figure 4. Thermoelectric properties as a function of temperature for $Pb_{0.975}Na_{0.025}S$ with 3.0% metal sulfides (CdS, ZnS, CaS, and SrS): (a) Electrical conductivity; inset shows the enlarged part of electrical conductivity at 750−923 K. (b) Seebeck coefficient. (c) Power factor. (d) Total thermal conductivity. (e) Lattice thermal conductivity. (f) Figure of merit, ZT; the combined uncertainty for all measurements involved in the calculation of ZT is less than 15%. Data for CaS and SrS are from ref 13.

750−923 K range, inset of Figure 4a, the CdS-containing sample retains nearly the same values as the control $Pb_{0.975}Na_{0.025}S$. The Seebeck coefficients show negligible changes regardless of metal sulfide added as second phase, reflecting the excellent control of the carrier concentrations through the fixed 2.5% Na doping content, Figure 4b. With the highest electrical conductivity and the same Seebeck coefficient, the sample with CdS shows the highest power factors in the entire temperature range of measurement, Figure 4c. On the other hand, the total thermal conductivities for ZnS, CaS, and SrS are at comparable levels and show the same trend as a function of temperature. The higher thermal conductivity of the CdS-containing sample reflects the larger contribution of the electronic thermal conductivity, Figure 4d.

The lattice thermal conductivities for all metal sulfides are remarkably low (for PbS materials), as seen in Figure 4e and Figure 5, underscoring the high efficacy of these binary sulfide nanostructures for strong scattering of phonons. On a percent basis, the drop in lattice thermal conductivities observed in the PbS matrix are larger than those seen in PbTe.[1,2] All ZT values continue to rise to the highest temperature of measurement ~923 K, achieving 1.3, 1.2, 1.1, and 1.1, respectively, for 3.0% content of CdS, ZnS, CaS, and SrS, Figure 4f. It is worth pointing out here that the heating and cooling cycles for the electrical and thermal properties measurements exhibited repeatable and consistent transport behavior, suggesting good thermal stability.

Valence Band Alignment between p-Type PbS Matrix and the Embedded Metal Sulfides. The best thermoelectric properties for p-type $Pb_{0.975}Na_{0.025}S$-x% MS (M = Cd, Zn, Ca,

dx.doi.org/10.1021/ja306527n | J. Am. Chem. Soc. 2012, 134, 16327−16336

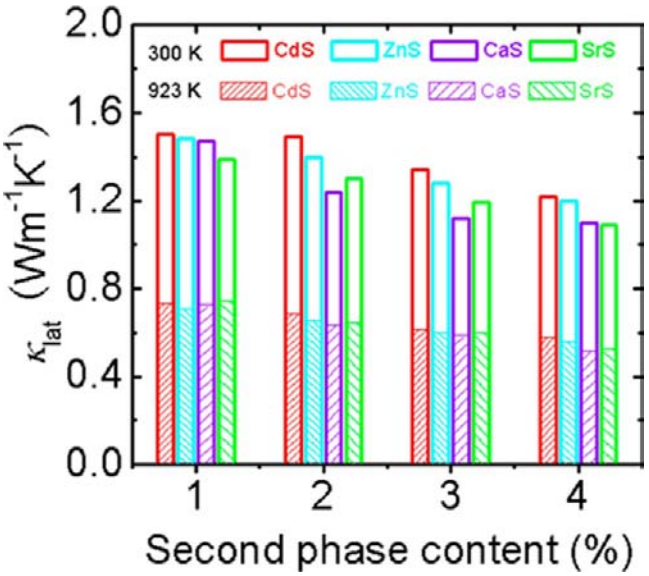

Figure 5. Lattice thermal conductivity for the p-type PbS with metal sulfides at room temperature and 923 K, respectively. Data for CaS and SrS are from ref 13.

Sr) samples are exhibited for M = Cd, Figure 4. As we discussed above, the lattice thermal conductivities are comparable for all systems and the superior ZT of the CdS-containing samples comes from a higher hole carrier mobility. It is useful to compare the effect of the second phases on both the electron (n-type) and hole (p-type) mobilities in PbS with CdS, ZnS, CaS, and SrS. As shown in Figure 6a, for n-type PbS, the electron mobility values at both room temperature and at 923 K are significantly reduced over the electron mobilities of pure n-type PbS, at their respective temperatures. The level of mobility reduction is almost the same regardless of the nature of metal sulfide. Here, the mobility at 923 K was calculated by assuming constant carrier concentration and using the electrical conductivity data at 923 K because in PbS only one band is involved in transport.[13] The significantly reduced electron mobility indicates relatively strong scattering of electrons in the conduction band of PbS, and it is explained by the DFT calculations of energy barriers caused by the large energy differences (>0.5 eV) between the conduction bands of PbS and those of the metal sulfides. Relative to PbS, these calculated conduction band energy differences are 0.54 eV, 0.91 eV, 1.09 eV, and 1.21 eV for CdS, ZnS, CaS, and SrS, respectively, as shown in Figure 6b. These are very large energy offsets that well exceed the magnitude of thermal energy at elevated temperature of kT. Here k is the Boltzmann constant and T is the absolute temperature;[27] for example, the thermal energy is about 0.086 eV at 1000 K.

For the p-type PbS case, the situation is very different and much more interesting. The hole mobilities of the CdS-containing p-type PbS samples are the highest, Figure 6c. Namely, the room temperature carrier mobility is ~184 cm^2 V^{-1} s^{-1} for the $Pb_{0.975}Na_{0.025}S$-1.0% CdS sample very close to that of the "control" sample, $Pb_{0.975}Na_{0.025}S$, of ~186 cm^2 V^{-1} s^{-1} with a similar carrier concentration of 4.78 × 10^{19} cm^{-3}, Figure 6c. The insertion of CdS nanocrystallines in the PbS matrix therefore does not appear to affect the hole scattering especially at elevated temperature. Two main factors are believed to be responsible for this: (a) a three-dimensional crystallographic endotaxial alignment of the two lattices with

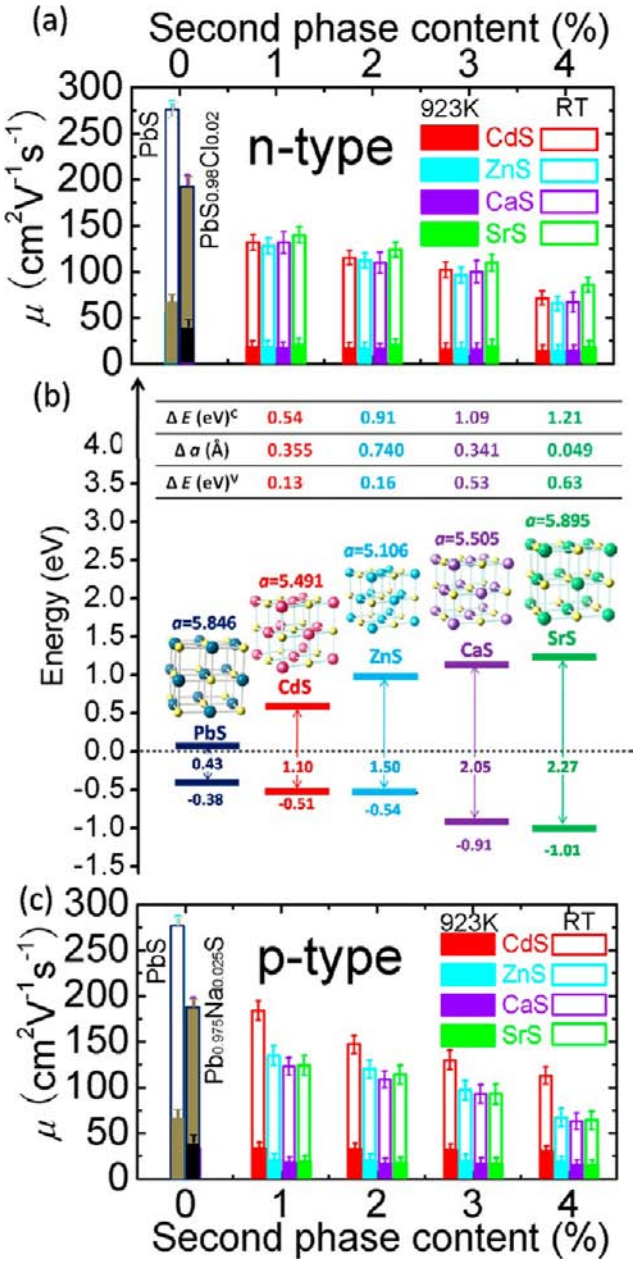

Figure 6. (a) Carrier mobility for the n-type PbS with metal sulfides at room temperature and 923 K, respectively. (b) DFT band alignments of the conduction band (CB) and valence band (VB) energy levels for PbS, CdS, ZnS, CaS, and SrS. All calculations are for metal sulfides in the NaCl structure. Δa represents the lattice parameters difference between PbS and other metal sulfides, ΔE^C (ΔE^V) represents the energy difference for the conduction (valence) bands between PbS and other metal sulfides. (c) Carrier mobility for the p-type PbS with metal sulfides at room temperature and 923 K, respectively. Data for CaS and SrS are from ref 13.

coherent/semicoherent interfaces (observed by TEM); (b) the better alignment of energies of the valence band maximum between PbS and CdS (in the NaCl structure). The electronic band structure calculations on PbS and the metal sulfides indicate that VBM energy differences (with respect to the VBM of PbS) are 0.13, 0.16, 0.53, and 0.63 eV for CdS, ZnS, CaS, and SrS, respectively, as shown in the inset table of Figure 6b. The minimum band offset is about 0.13 eV at 0 K with the valence band maximum of PbS lying lower than that of CdS,

dx.doi.org/10.1021/ja306527n | J. Am. Chem. Soc. 2012, 134, 16327−16336

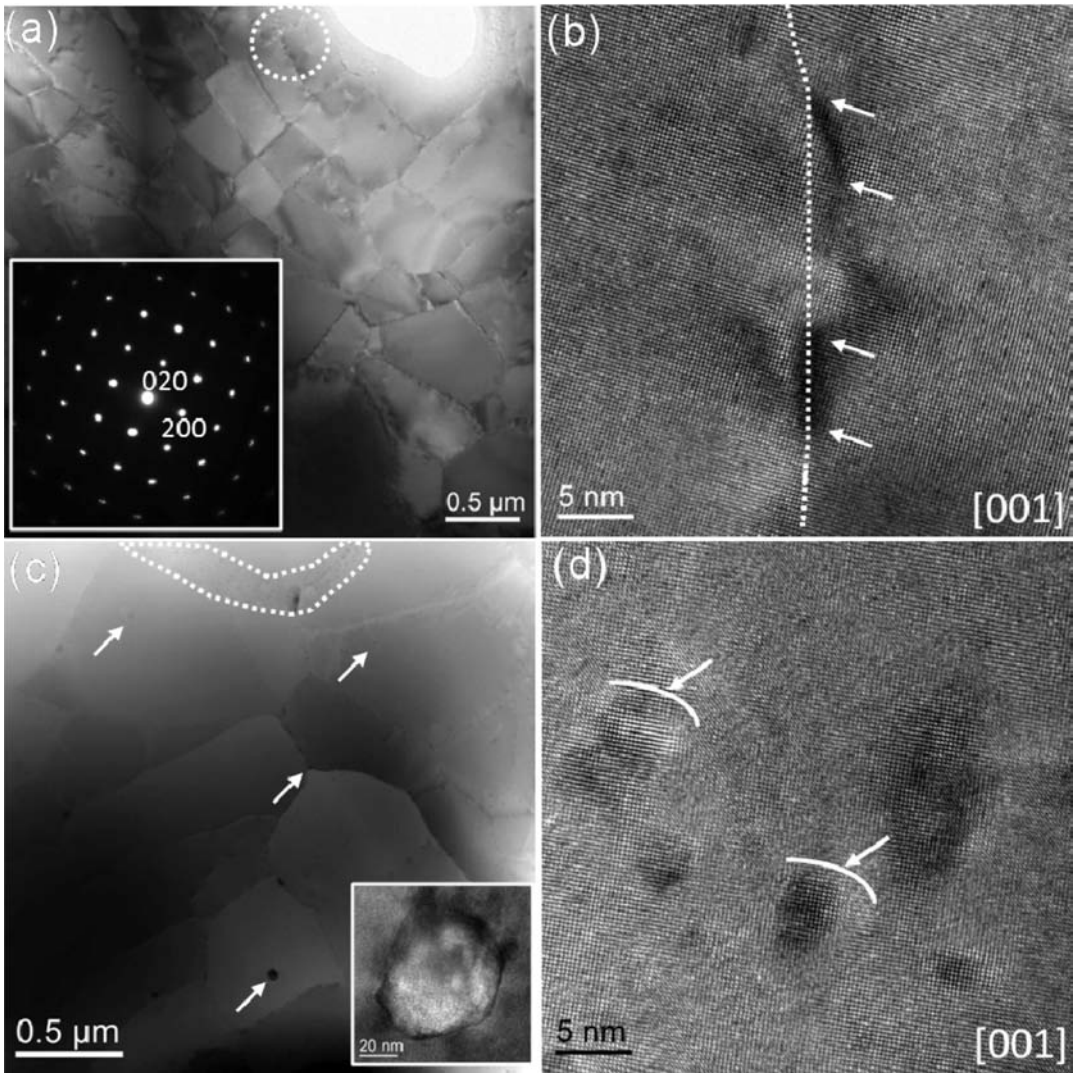

Figure 7. (a) Low magnification TEM image of $Pb_{0.975}Na_{0.025}S$ with 3.0% ZnS; inset shows an electron diffraction pattern coming from several grains. (b) HRTEM image showing perfect alignment between two PbS grains. (c) STEM image showing some dark contrast. (d) HRTEM image depicting low number density nanoscale precipitates.

which in turn is lower than those of the other metal sulfides. The band offsets are expected to decrease with rising temperature due to thermal band broadening, further facilitating carrier transmission across the interface. The degree of hole carrier scattering is expected to scale with the size of the valence band offsets between PbS and metal sulfides, and this is in fact what is observed across this metal sulfide family.

Transmission Electron Microscopy. Two typical samples, $Pb_{0.975}Na_{0.025}S$-3.0% ZnS and $Pb_{0.975}Na_{0.025}S$-3.0% CdS (both exhibiting the highest *ZT* in each system) were studied with TEM in detail. Figure 7a is a characteristic low-magnification TEM image of the $Pb_{0.975}Na_{0.025}S$-3.0% ZnS sample which clearly shows grains of the PbS matrix with an average size of 0.8 μm. The inset is an electron diffraction pattern along the nominal [001] PbS direction from the selected area aperture that can be readily indexed for cubic PbS. The spots in this electron diffraction pattern show small elongation and arcs rather than splitting or significant rotation, suggesting crystalline alignment among the domains. The high resolution TEM (HRTEM) image in Figure 7b shows a semicoherent and low-angle grain boundary outlined by white dotted line between these two PbS grains. The grain boundary consists of misfit dislocations and stacking faults separating two partial dislocations as indicated at the end of white arrowheads. In Figure 7c, the scanning TEM (STEM) image with magnification similar to that in Figure 7a provides better contrast and shows random distribution of irregularly sized precipitates. The presence of one set of Bragg spots for both precipitates and matrix confirm that these precipitates are lattice-matched, isostructural to PbS with endotaxially orientation. EDS spectra of the precipitates, Figure S7a in Supporting Information, confirm they are ZnS. Some regions have low number density midsize precipitates (~15−60 nm, enlarged region shown in the inset) with dark strain contrast identified by arrowheads while other regions have high number density of much smaller size nanoscale precipitates (~1−8 nm) marked by a dotted line, which can also be seen in the high magnification image, Figure 7d. On average, the HRTEM images clearly reveal that the number density of the nanoscale precipitates is lower than those found in corresponding CdS-containing samples (below) and other previously studied PbS-based systems.[12,13]

Figure 8a is a low magnification TEM image from a $Pb_{0.975}Na_{0.025}S$-3.0% CdS sample and reveals little larger average grain size (~1.0−1.2 μm) and higher number density of

dx.doi.org/10.1021/ja306527n | *J. Am. Chem. Soc.* 2012, 134, 16327−16336

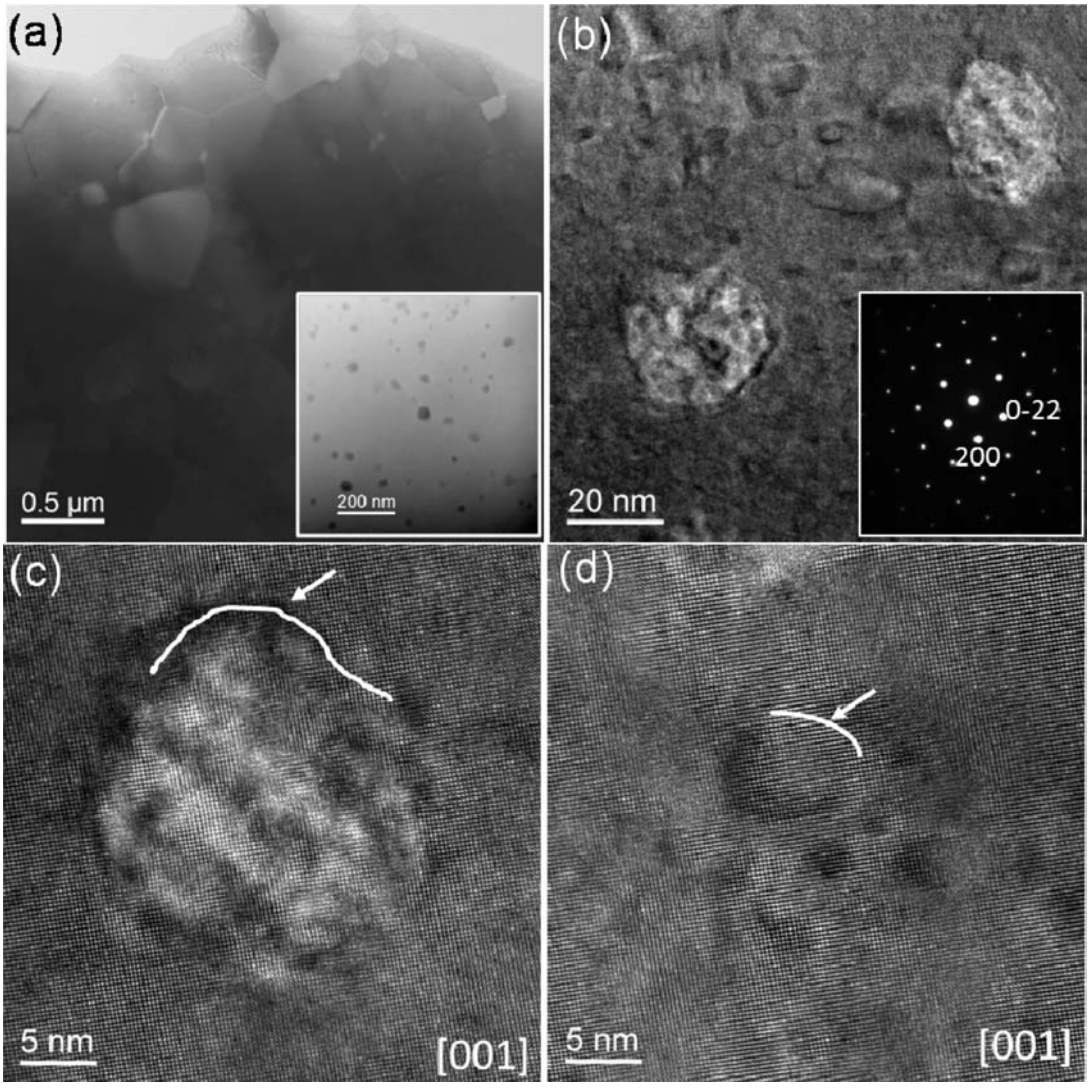

Figure 8. (a) Low magnification TEM image of $Pb_{0.975}Na_{0.025}S$ with 3.0% CdS; inset, the STEM image shows high number density nanostructures. (b) Middle magnification TEM image showing both type size nanostructures, 20−50 nm and 2−10 nm; inset, the corresponding diffraction pattern along the [011] direction does not show any spot splitting. (c and d) HRTEM images of bigger and smaller nanoscale precipitates, respectively.

nanoscale precipitates than in the 3.0% ZnS-containing sample; see inset in Figure 8a. This image shows that the midsize nanostructures have a size range from 20 to 50 nm. The midmagnification image in Figure 8b further shows smaller nanoscale precipitates in the range of ∼2−10 nm. Energy dispersive X-ray spectroscopy (EDS) spectra of the precipitates, Figure S7b, confirm they are CdS. The electron diffraction pattern (inset) taken with an aperture including two different size precipitates and matrix show only one set of spots, which means the PbS matrix and nanoscale precipitates have similar symmetry, structure, and lattice parameters and are endotaxially aligned. Figure 8c is an HRTEM image depicting several coherent and semicoherent interfaces between the larger precipitate and the matrix. Figure 8d shows coherent precipitate/matrix interfaces for smaller size precipitates.

Overall, the TEM observations of these two types of samples reveal a typical combination of low-/high-angle grain boundaries, matrix dislocations, nanoscale precipitates, and associated coherent (for smaller size precipitates) or semicoherent (for larger size precipitates) interfaces. Second-phase precipitates larger than >60 nm were not observed.[28] All these will affect electron and phonon scattering differently because they have diverse scattering properties. We believe that the diversity of scattering mechanism for phonons in such nanostructured thermoelectrics, coupled with endotaxial orientation of nanoscale precipitates, collectively contribute toward higher *ZT* values in this important PbS matrix system. The overall operating concept that is the key to the generic design of high *ZT* thermoelectrics is shown in Figure 9.

■ CONCLUDING REMARKS

The thermoelectric performance of the PbS system and, by extension, other systems can be enhanced by means of a closely coupled phonon-blocking/electron-transmitting approach through embedding endotaxially nanostructured second phases. Our work shows that the figure of merit *ZT* of p-type PbS can be increased to the record high value of ∼1.3 at 923 K with CdS nanostructures. Although the same strong reduction of the lattice thermal conductivity is achieved with ZnS, CaS, and SrS, the enhanced *ZT* of the CdS system derives from better hole mobility. The higher hole mobility is explained by first-principles density functional theory calculations which indicate

dx.doi.org/10.1021/ja306527n | *J. Am. Chem. Soc.* 2012, 134, 16327−16336

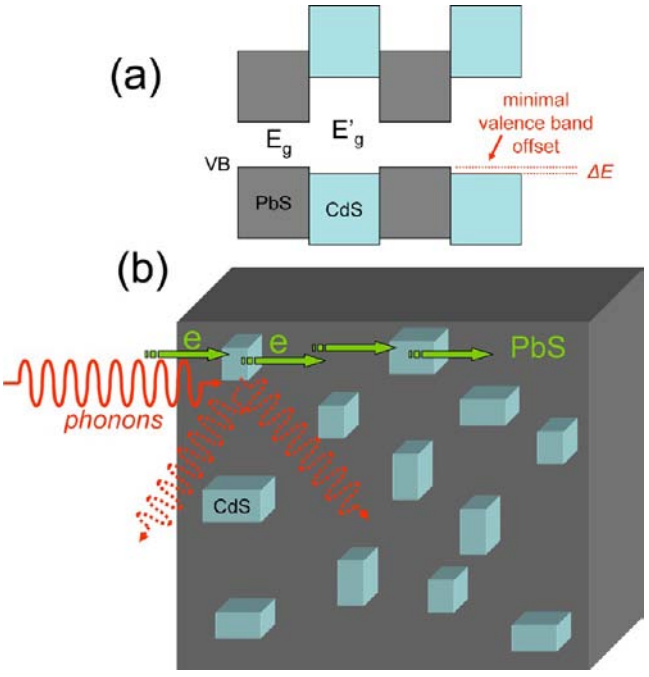

Figure 9. (a) Relative energy band diagram for the combined nanostructured PbS-*x*% CdS system showing the large differences in semiconducting band gap and small energy difference, ΔE, in the valence band edges. (b) The small valence band offsets allow facile hole transmission through a nanostructured material with an endotaxially arranged second phase that simultaneously scatters heat-carrying phonons at the matrix/nanostructure interface.

that the valence band offsets between PbS and CdS are the smallest at 0.13 eV compared to those between PbS and ZnS, and CaS or SrS. The small offsets allow facile hole transport through the material by presenting small energy barriers for carrier crossing from matrix to nanostructure and vice versa. The present results confirm that higher thermoelectric performance can be realized in bulk p-type PbS with endotaxial placement of judiciously chosen second phases to engineer proper electronic band alignment. Theoretical guidance can play a key role in the future application of this concept in helping to identify suitable phase pairs. Finally, we point out that PbS contains the least expensive elements among any high *ZT* thermoelectric materials under consideration today, including $Mg_2Si_{1-x}Sn_x$.[1,2] Clearly, the great environmental stability of PbS as evidenced by the ubiquitous mineral galena, coupled with ease of fabrication and high thermoelectric performance for both n-type and p-type doping, make nanostructured PbS competitive with all other premier high temperature thermoelectrics such as the heavier lead chalcogenides, filled skutterudites, magnesium silicide, and silicon–germanium alloys.

■ ASSOCIATED CONTENT

Supporting Information

Density of samples included in the study (Table S1). Powder XRD patterns and lattice parameters of $Pb_{0.975}Na_{0.025}S$ with *x* % ZnS (Figure S1). Electronic absorption spectra of different PbS samples with ZnS and without Na doping (Figure S2). Thermoelectric properties as a function of temperature for $Pb_{0.975}Na_{0.025}S$ with *x* % ZnS including heat capacity, thermal diffusivity, Lorenz number, and electronic thermal conductivity (Figure S3). Powder XRD patterns and lattice parameters of $Pb_{0.975}Na_{0.025}S$ with *x* % CdS (Figure S4). Electronic absorption spectra of different PbS samples with CdS and without Na doping (Figure S5). Thermoelectric properties as a function of temperature for $Pb_{0.975}Na_{0.025}S$ with *x* % CdS including heat capacity, thermal diffusivity, Lorenz number, and electronic thermal conductivity (Figure S6). EDS spectra from matrix and precipitate for the $Pb_{0.975}Na_{0.025}S$ with 3.0% ZnS and 3.0% CdS (Figure S7). Formation energy of interstitial hydrogen as a function of Fermi level in PbS (Figure S8) and the calculation details. Calculated band gaps of interested metal sulfides (Figure S9). This material is available free of charge via the Internet at http://pubs.acs.org.

■ AUTHOR INFORMATION

Corresponding Author

m-kanatzidis@northwestern.edu

Notes

The authors declare no competing financial interest.

■ ACKNOWLEDGMENTS

This work was supported in part by a grant DOE-EERE/NSF (CBET-1048728) (L.D.Z. and M.G.K.). The transmission electron microscopy, spark plasma sintering, and density functional calculations in this work were supported as part of the Revolutionary Materials for Solid State Energy Conversion, an Energy Frontier Research Center funded by the U.S. Department of Energy, Office of Science, and Office of Basic Energy Sciences under Award Number DE-SC0001054 (J.H., S.H., C.I.W., C.W., T.P.H., and V.P.D.). Transmission electron microscopy work was performed in the (EPIC) (NIFTI) (Keck-II) facility of NU*ANCE* Center at Northwestern University. The NU*ANCE* Center is supported by NSF-NSEC, NSF-MRSEC, Keck Foundation, the State of Illinois, and Northwestern University. We acknowledge use of the Office of Naval Research DURIP-supported Pulsed Electric Current Sintering System at Michigan State University.

■ REFERENCES

(1) (a) Kanatzidis, M. G. *Chem. Mater.* **2010**, *22*, 648. (b) Sootsman, J. R.; Chung, D.-Y.; Kanatzidis, M. G. *Angew. Chem., Int. Ed.* **2009**, *48*, 8616. (c) Kanatzidis, M. G. *Semicond. Semimetals* **2000**, *69*, 51. (d) Vineis, C. J.; Shakouri, A.; Majumdar, A.; Kanatzidis, M. G. *Adv. Mater.* **2010**, *22*, 3970.

(2) (a) Li, J.-F.; Liu, W. S.; Zhao, L.-D.; Zhou, M. *NPG Asia Mater.* **2010**, *2*, 152. (b) Snyder, J. G.; Toberer, E. S. *Nat. Mater.* **2008**, *7*, 105. (c) Chen, G.; Dresselhaus, M. S.; Dresselhaus, G.; Fleurial, J.-P.; Caillat, T. *Int. Mater. Rev.* **2003**, *48*, 45. (d) Dresselhuas, M. S.; Chen, G.; Tang, M.; Yang, R.; Lee, H.; Wang, D.; Ren, Z.; Fleurial, J.; Gogna, P. *Adv. Mater.* **2007**, *19*, 1043. (e) Zebarjadi, M.; Esfarjani, K.; Dresselhaus, M. S.; Ren, Z. F.; Chen, G. *Energy Environ. Sci.* **2012**, *5*, 5147. (f) Bilc, D.; Mahanti, S. D.; Quarez, E.; Hsu, K. F.; Pcionek, R.; Kanatzidis, M. G. *Phys. Rev. Lett.* **2004**, *93*, 146403.

(3) Hsu, K. F.; Loo, S.; Guo, F.; Chen, W.; Dyck, J. S.; Uher, C.; Hogan, T.; Polychroniadis, E. K.; Kanatzidis, M. G. *Science* **2004**, *303*, 818.

(4) (a) Quarez, E.; Hsu, K. F.; Pcionek, R.; Frangis, N.; Polychroniadis, E. K.; Kanatzidis, M. G. *J. Am. Chem. Soc.* **2005**, *127*, 9177. (b) Poudeu, P. F. P.; D'Angelo, J.; Kong, H. J.; Downey, A.; Short, J. L.; Pcionek, R.; Hogan, T. P.; Uher, C.; Kanatzidis, M. G. *J. Am. Chem. Soc.* **2006**, *128*, 14347. (c) Sootsman, J. R.; Pcionek, R. J.; Kong, H. J.; Uher, C.; Kanatzidis, M. G. *Chem. Mater.* **2006**, *18*, 4993.

(5) Zhou, M.; Li, J.-F.; Kita, T. *J. Am. Chem. Soc.* **2008**, *130*, 4527.

(6) Androulakis, J.; Hsu, K. F.; Pcionek, R.; Kong, H.; Uher, C.; D'Angelo, J. J.; Downey, A.; Hogan, T.; Kanatzidis, M. G. *Adv. Mater.* **2006**, *18*, 1170.

(7) Poudeu, P. F. P.; D'Angelo, J. J.; Downey, A. D.; Short, J. L.; Hogan, T. P.; Kanatzidis, M. G. *Angew. Chem., Int. Ed.* **2006**, *45*, 3835.
(8) (a) Androulakis, J.; Lin, C.-H.; Kong, H.-J.; Uher, C.; Wu, C.-I.; Hogan, T.; Cook, B. A.; Caillat, T.; Paraskevopoulos, K. M.; Kanatzidis, M. G. *J. Am. Chem. Soc.* **2007**, *129*, 9780. (b) Girard, S. N.; He, J. Q.; Zhou, X. Y.; Shoemaker, D.; Jaworski, C. M.; Uher, C.; Dravid, V. P.; Heremans, J. P.; Kanatzidis, M. G. *J. Am. Chem. Soc.* **2011**, *133*, 16588. (c) He, J. Q.; Girard, S. N.; Kanatzidis, M. G.; Dravid, V. P. *Adv. Funct. Mater.* **2010**, *20*, 764.
(9) Ahn, K.; Han, M. K.; He, J. Q.; Androulakis, J.; Ballikaya, S.; Uher, C.; Dravid, V. P.; Kanatzidis, M. G. *J. Am. Chem. Soc.* **2010**, *132*, 5227.
(10) Androulakis, J.; Todorov, I.; He, J. Q.; Chung, D.-Y.; Dravid, V. P.; Kanatzids, M. G. *J. Am. Chem. Soc.* **2011**, *133*, 10920.
(11) Johnsen, S.; He, J. Q.; Androulakis, J.; Dravid, V. P.; Todorov, I.; Chung, D.-Y.; Kanatzidis, M. G. *J. Am. Chem. Soc.* **2011**, *133*, 3460.
(12) Zhao, L.-D.; Lo, S.-H.; He, J. Q.; Li, H.; Biswas, K.; Androulakis, J.; Wu, C.-I.; Hogan, T. P.; Chung, D.-Y.; Dravid, V. P.; Kanatzidis, M. G. *J. Am. Chem. Soc.* **2011**, *133*, 20476.
(13) Zhao, L.-D.; He, J. Q.; Wu, C.-I.; Hogan, T. P.; Zhou, X. Y.; Uher, C.; Dravid, V. P.; Kanatzidis, M. G. *J. Am. Chem. Soc.* **2012**, *134*, 7902.
(14) Zhao, L.-D.; Zhang, B. P.; Li, J.-F.; Zhou, M.; Liu, W.-S.; Liu, J. *J. Alloys Compd.* **2008**, *455*, 259.
(15) Zhao, X. Y.; Shi, X.; Chen, L. D.; Zhang, W. Q.; Bai, S. Q.; Pei, Y. Z.; Li, X. Y.; Goto, T. *J. Appl. Phys.* **2006**, *89*, 092121.
(16) Sootsman, J. R.; Kong, H. J.; Uher, C.; D'Angelo, J. J.; Wu, C. T.; Hogan, T. P.; Caillat, T.; Kanatzidis, M. G. *Angew. Chem., Int. Ed.* **2008**, *47*, 8618.
(17) Li, H.; Tang, X. F.; Su, X. L.; Zhang, Q. J. *Appl. Phys. Lett.* **2008**, *92*, 202114.
(18) Kim, W.; Zide, J.; Gossard, A.; Klenov, D.; Stemmer, S.; Shakouri, A.; Majumdar, A. *Phys. Rev. Lett.* **2006**, *96*, 045901.
(19) Venkatasubramanian, R.; Siivola, E.; Colpitts, V.; O'Quinn, B. *Nature* **2001**, *413*, 597.
(20) Biswas, K.; He, J. Q.; Zhang, Q. C.; Wang, G. Y.; Uher, C.; Dravid, V. P.; Kanatzidis, M. G. *Nat. Chem.* **2011**, *3*, 160.
(21) Blachnik, R.; Igel, R. *Z. Naturforsch. B* **1974**, *29*, 625.
(22) Perdew, J. P.; Burke, K.; Ernzerhof, M. *Phys. Rev. Lett.* **1996**, *77*, 3865.
(23) Kresse, G.; Furthmüller, J. *Phys. Rev. B* **1996**, *54*, 11169.
(24) Van de Walle, C. G.; Neugebauer, J. *Nature* **2003**, *423*, 626.
(25) Van de Walle, C. G.; Neugebauer, J. *J. Appl. Phys.* **2004**, *95*, 385.
(26) (a) Fitsul, V. I. *Heavily Doped Semiconductors*; Plenum Press: New York, 1969. (b) Ravich, I. I.; Efimova, B. A.; Smirnov, I. A. *Semiconducting lead chalcogenides*; Plenum Press: New York, 1970.
(27) Fang, F.; Opila, R. L.; Venkatasubramanian, R.; Colpitts, T. *J. Vac. Sci. Technol.* **2011**, *A29*, 031403.
(28) (a) Pei, Y. Z.; Heinz, N. A.; LaLonde, A.; Snyder, G. J. *Energy Environ. Sci.* **2011**, *4*, 3640. (b) Pei, Y. Z.; LaLonde, A.; Heinz, N. A.; Snyder, G. J. *Adv. Energy Mater.* **2012**, *2*, 670.